RSC Advances

PAPER

Cite this: *RSC Adv.*, 2015, **5**, 82282

The reducibility of highly stable Ni-containing species in catalysts derived from hydrotalcite-type precursors

Ida Pettiti,[a] Delia Gazzoli,[a] Patricia Benito,*[b] Giuseppe Fornasari[b] and Angelo Vaccari[b]

Received 14th July 2015
Accepted 21st September 2015

DOI: 10.1039/c5ra13863a

www.rsc.org/advances

A study was conducted on the speciation and reducibility of Ni in catalysts derived from hydrotalcite-type (HT) precursors intercalated by silicates. Silicate and nickel contents in Ni/Mg/Al HT precursors varied and the products obtained by thermal decomposition in the 773–1373 K range were characterized. Sample properties were related to the amount of silicates and nickel. The former altered the formation of the spinel-type phase and decreased the ratio between MgO and $MgAl_2O_4$ phases in which the active species were stabilized. On the other hand, the Ni distribution depended on the Ni-loading. Ni-containing species in the spinel phase were more abundant for high Ni-loaded catalysts, and were readily reduced by H_2 treatment at 1023 K, whereas those in the $Ni_{1-x}Mg_xO$ solid solution remained partially unreduced.

1. Introduction

Ever since the late 1990s, Ni-containing hydrotalcite-type (HT) precursors have been widely used to prepare highly active and stable catalysts for the production of H_2 and syngas ($CO + H_2$) from fossil fuels by reforming (steam,[1,2] autothermal,[3] dry[4–9]) or partial oxidation.[10–13] The main advantages of HT-derived catalysts stem from the dispersion of Ni^{2+} in an oxide matrix, with a basic character and a relatively high surface area. Metallic particles responsible for the reagent activation, formed by reduction, are highly dispersed and stable toward sintering even for high nickel loadings,[14] due to the confinement of the nickel in mixed-oxide nanoribbons.[15] Thus HT-derived catalysts outperformed conventional and commercial catalysts in terms of activity, stability toward sintering, and reduced carbon formation.[2,5,15] Thanks to their features, in recent years they have also found application in the reforming of ethanol,[16,17] which is more prone to carbon formation, and complex renewable feedstocks, such as biogas[18,19] or tars,[20,21] which are present in biomass gasification streams.

The versatility of HT-derived catalysts is related to the structure and chemical composition of HT precursors. They are lamellar materials with the general chemical formula $[M^{2+}_{1-x}M^{3+}_x(OH)_2]\cdot(A^{n-})_{x/n}\cdot H_2O$,[22] showing a brucite-type structure. In the CdI_2-type layered structure of $Mg(OH)_2$ a partial replacement of Mg^{2+} by trivalent cations (for example Al^{3+}) occurs, whereas the charge excess is balanced by the anions (A^{n-}), which for catalytic purposes are usually CO_3^{2-}, located in the interlayer region together with water molecules. The topotactical thermal decomposition of HT phases is responsible for the relationship between precursor nature and catalyst properties. Since the first Ni/Al–CO_3 HT formulation used as precursor of a steam reforming catalyst in the early 1975,[23] many chemical compositions have been suggested to improve catalyst performances. The most common approach involved the replacement of Ni^{2+} by Mg^{2+}, obtaining Ni/Mg/Al–CO_3 precursors, as suggested by some of us.[10,24] Noble metals,[25] Fe,[20,26] or Co[27] were also introduced into brucite-type layers to obtain bimetallic particles. Moreover, La, Ce, Pr, and Ca can be added to the formulation.[8,28–30]

HT decomposition temperature determines the crystalline phases in the catalyst, Ni speciation,[7,24,31–33] Ni dispersion, reduction–oxidation behavior, surface area, and acid–base properties. At 723–1023 K, a rock salt-type phase with high surface area was identified by XRD, containing Mg^{2+}, Ni^{2+}, and Al^{3+}.[31] The metal–support interaction is high and a complete $Ni^{2+} \rightarrow Ni^0$ reduction can be achieved by H_2 treatment; however, the catalyst may be modified with time-on-stream in the reactor if the calcination temperature is exceeded. Therefore, for high-temperature catalytic processes, HT precursors should be treated at a temperature suitable for preparing stable materials. For example, at 1173 K, rock salt-type and spinel-type phases segregated and the catalyst did not suffer from the thermal sintering during the catalytic partial oxidation (CPO) of CH_4.[13] Ni^{2+} species were reported to be present as NiO, $Mg_{1-x}Ni_xAl_2O_4$, and $Mg_{1-x}Ni_xO$ crystalline phases, depending on the Ni content.[4] In high-temperature calcined

[a]*Dip.to Chimica, Università degli Studi di Roma "La Sapienza", P.le A. Moro 5, Roma, 00185, Italy*

[b]*Dipartimento Chimica Industriale "Toso Montanari", Alma Mater Studiorum – Università di Bologna, Viale Risorgimento 4, Bologna, 40136, Italy. E-mail: patricia.benito3@unibo.it; Fax: +39 0512093679; Tel: +39 0512093677*

samples, the metal–support interaction was strong, mainly for low Ni-loaded catalysts, but the reducibility decreased. XANES/EXAFS studies revealed that only part of the Ni^{2+} species was reduced in Ni/Mg/Al compounds, however without any Ni speciation.[34] The change in the reduction temperature or activation with time-on-stream minimized the amount of unreduced species.[12]

Last but not least, regardless of the calcination temperature, the Mg^{2+}/Al^{3+} ratio and Ni content are important parameters to be tuned, since they determine not only the nature of the crystalline phases in which Ni is solved and its reducibility, but also the basic character of the support.[1,12,32,35–38]

In previous works, some of us reported on an alternative way to modify HT-derived CPO catalyst properties, consisting of the incorporation of silicate anions in the interlayer region during the HT precursor synthesis.[13,39] This approach has also been extended to the preparation of catalysts for the synthesis of 1-phenoxy-2-propanol feeding phenol and propylene oxide[40] and to the oxidation of alcohols to aldehydes.[41] By using silicate-intercalated HT compounds for the preparation of Ni-containing CPO catalysts, the forsterite phase (Mg_2SiO_4) formed by calcination at 1173 K not only enhanced the catalyst's mechanical stability, but also altered its crystalline components and their activity in the partial oxidation of CH_4.[13] After an activation with time-on-stream a 8 wt% Ni catalyst showed good performances, which slightly depended on the silicate amount; while a 2 wt% Ni catalyst deactivated with time-on-stream by increasing the silicate content. XPS[13] and CO-DRIFT[42] analyses revealed that some Ni^{2+} or $Ni^{\delta+}$ species were present in the reduced catalyst before CPO tests, decreasing the amount of available Ni^0 active species (also confirmed by H_2 chemisorption). These species were reduced with time-on-stream for the 8 wt% Ni catalyst, but metallic particle sizes remained almost constant (from 12.1 to 10.5 nm) after CPO tests.[42]

In silicate-containing HT-derived catalysts, the distribution of Ni^{2+} species may vary in comparison to conventional carbonate-intercalated catalysts. Some Mg^{2+} ions were used in the forsterite phase, thus altering the rock salt/spinel ratio. XPS suggested that Ni species in calcined samples could be inserted in both crystalline phases;[13] however, an accurate Ni speciation in calcined and reduced catalysts is still lacking.

The aim of this work was to elucidate the role of silicates and Ni loading on both the formation of crystalline phases and the reducibility of Ni species, in order to tailor the properties of HT-derived Ni-silicate-containing catalysts. Firstly, the thermal decomposition of Ni-HT phases intercalated with different amounts of silicate was investigated, focusing on the effect of silicates on the formation of crystalline phases, the reducibility of Ni species and the specific surface area of the samples. Secondly, the reducibility and speciation of Ni were studied in the actual catalysts, previously used in the CPO of CH_4,[13] namely in samples obtained from HT precursors intercalated with 20% excess of silicates and calcined at 1173 K, to complete the characterization and explain their catalytic performances.

2. Experimental

2.1. Synthesis of the catalysts

Silicate-containing samples were prepared by coprecipitation at constant pH;[13] a 2 M solution containing $Ni(NO_3)_2 \cdot 6H_2O$, $Mg(NO_3)_2 \cdot 6H_2O$ and $Al(NO_3)_3 \cdot 9H_2O$ in the appropriate ratios was slowly added to a 1 M solution containing silicates [sodium silicate solution, NaOH (≥10%), SiO_2 (≥27%), Aldrich]. The atomic ratios (a.r.%) used in this work were: Ni/Mg/Al = 0/68/32, 2/66/32, 8/60/32, 15/53/32 and 68/0/32. The amount of silicates corresponded to 20 or 62% excess, to balance the charge excess in the layers. The pH was kept constant by dropwise NaOH addition (10.5 ± 0.2). The obtained precipitate was kept in suspension under stirring at 323 K for 45 min, then filtered and washed with distilled water until a Na_2O content lower than 0.02 wt% was obtained. Then the precipitate was dried overnight at 323 K.

To shed light on the thermal evolution of HT precursors, the precipitated samples were calcined at 10 K min^{-1} up to selected temperatures (773, 1023, 1073, 1123, 1173, 1223, 1273, 1323, and 1373 K), keeping these values for 12 h. Another, more detailed structural characterization was performed to determine the Ni speciation by focusing on samples obtained by calcination, at 1173 K for 12 h, of the HT precursors containing 20% excess of silicates.

Ni catalysts were labelled: Ni*x*, where *x* referred to the a.r.%, *i.e.* Ni0, Ni2, Ni8, Ni15 and Ni68 for Ni/Mg/Al = 0/68/32, 2/66/32, 8/60/32, 15/53/32, 68/0/32 a.r.% respectively.

For comparison purposes, a Ni/Al-HT precursor containing carbonates was prepared (Ni/Al = 68/32 a.r.%) and calcined at 1173 K (Ni68–CO_3).

2.2. Characterization

X-Ray Diffraction (XRD) powder analyses of the samples calcined at different temperatures were carried out using a Philips PW1050/81 diffractometer equipped with a graphite monochromator in the diffracted beam and controlled by a PW1710 unit (λ = 0.15418 nm). A 2θ range from 10° to 80° was investigated (step size 0.1°; time per step 2.00 s). XRD patterns of the samples with different Ni loading calcined at 1173 K were obtained by using a Philips PW 1729 diffractometer, interfaced to a computer for data acquisition and analysis (software APD-Philips), using a Ni-filtered CuKα radiation. Diffraction patterns were recorded in the 2θ range from 3° to 80° for phase analysis (step size 0.02°; time per step 1.25 s) and in the 90–148° 2θ range for lattice parameter determinations (step size 0.02°; time per step 5.00 s). Lattice parameters for the MgO unit cell were calculated by using the UNITCELL software[43] using the following reflections: (400), $2\theta = 94°$; (420), $2\theta = 110°$; (422), $2\theta = 127°$.

Specific surface area assessment was carried out using a Micromeritics ASAP 2020 instrument; calcined solids were heated up to 423 K and evacuated at a pressure better than 0.02 Torr, kept for 30 min at this temperature, and lastly heated up to 523 K and kept there for 30 min.

Temperature programmed reduction and oxidation analyses were carried out by feeding a H_2/He = 5/95 v/v or a O_2/N_2 = 5/95

v/v gas mixture (flow rate 20 mL min^{-1}) in the 333–1223 K temperature range, with a heating ramp of 10 K min^{-1} in a ThermoQuest CE instruments TPDRO 1100.

XPS spectra were collected using a Leybold-Heraeus LHS10 spectrometer operating in FAT mode (50 eV pass energy), using a twin AlKα (12 kV/20 mA) and MgKα (10 kV/20 mA) anode at a pressure below 10^{-9} Torr. The samples, reduced to fine powders, were manually pressed onto a double-sided adhesive tape attached to the sample rod. Samples were reduced under the same conditions as for catalytic tests,[13] namely with a H_2/N_2 = 50/50 v/v gas mixture at 1023 K for 12 h. Reduction treatments *in situ* in a flowing H_2/N_2 = 10/90 v/v gas mixture (flow rate 6 mL min^{-1}) at 723 K for 4 h were carried out in a side apparatus which was directly connected to the preparation chamber. The actual sample temperature was monitored by a thermocouple touching its surface. After being cooled down gradually to room temperature in the H_2/N_2 stream, the sample was transferred *in vacuo* to the preparation chamber and then sent into the analysis chamber for spectra collection. Ni2p, C1s, O1s, Si2s, Al2s, Si2p, Mg2s, Al2p and Mg2p regions were sequentially acquired. Binding energies (BE) were referenced to C1s at 285.0 eV and measured with an accuracy of ±0.2 eV. Data analysis involved smoothing, non-linear Shirley-type background subtraction and curve-fitting and peak areas by the integration of the appropriate peak by Esca Tools 4.2 software (Surface Interface Inc.). Because Al2p peak overlaps with the Ni3p signal, and Al2s with Ni3s, their contributions were determined by curve-fitting procedures. Changes in Ni2p signal shape on reduced samples were analyzed by curve-fitting procedures with Ni2p doublets endowed with fixed spectroscopic parameters ($Ni2p_{3/2}$–$2p_{1/2}$), spin–orbit separation 17.2 eV, and intensity ratio R = 0.50, but using variable position, full width at half maximum (FWHM), and intensities. Surface composition was obtained from peak area ratios by using the elemental sensitivity factors method.[44]

XAS spectra were recorded on the Ni K-edge, in the 8130–9600 eV range, at the beamline ELETTRA XAFS, (Trieste, Italy) in the transmission mode. The beamline monochromator was equipped with a Si (111) crystal. Measurements were performed at the liquid N_2 temperature on powder samples mixed with an appropriate amount of boron nitride and pressed into pellets. Measurements were taken on both calcined and reduced samples. XAS spectra of the reference compounds NiO, $NiAl_2O_4$, and Ni metal were also recorded. XAS data were processed using the "IFEFFIT" code package.[45] The XANES part of the experimental signal was obtained by subtracting a linear pre-edge and normalizing it to one in correspondence with the first EXAFS oscillation. Fourier transforms (FTs) of EXAFS data were carried out in the 2.5–16.0 $Å^{-1}$ k-range, by using a Kaiser–Bessel window, after weighting data by k^3. Structural information on the first coordination shell was obtained by back-transforming and fitting the FT function in the 1.0–2.0 Å range for oxidized samples and in the 1.5–2.5 Å range for reduced samples. Fits were performed using the theoretical phase and amplitude functions generated by the FEFF6 code. These functions were calibrated by the EXAFS spectra of reference compounds. For all the fits, the calculated statistical errors related to the bond distances were smaller than the uncertainty (0.02 Å) attributed to the EXAFS technique; for coordination numbers the inaccuracy was typically evaluated at around 10%.

3. Results and discussion

3.1. Role of silicates during the calcination of HT precursors

The calcination of Ni8 HT precursors with 20% and 62% excess of silicates in the 773–1373 K range was studied. Diffraction patterns were collected in 50 K steps to identify phase changes; however, only the patterns of samples calcined at 773, 1023, 1073, 1173, and 1373 K appear in Fig. 1a and b as representative for the study of the evolution of crystalline phases.

The dehydration, dehydroxylation, and collapse of the layered structure at 773 K gave rise to a scarcely crystallized rock-salt mixed oxide, in which Ni^{2+} and Al^{3+} were included.[31] The bump in the 20–30° 2θ range was related to amorphous silica. After treatment at 1023 K, no significant modifications took place, whereas at 1073 K forsterite (Mg_2SiO_4) crystallized

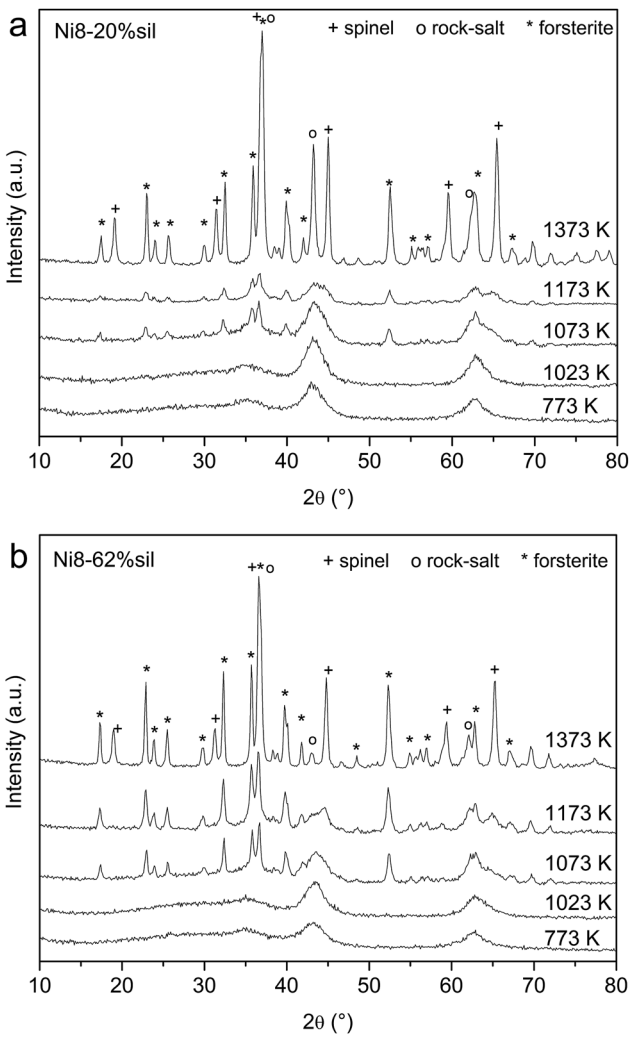

Fig. 1 XRD patterns of Ni/Mg/Al = 8/60/32 a.r.% samples containing 20% (a) and 62% (b) excess of silicates and calcined in the 773–1373 K range.

and at 1123 K (pattern not shown) a $MgAl_2O_4$-type phase was also present. Calcinations at 1173 K yielded no phases other than MgO-type, spinel-type, and forsterite. In the spinel pattern, the two reflections at $2\theta = 19°$ and 32° ascribed to (111) and (220) planes were not observed, thus suggesting the formation of a defective and/or disordered phase.[46] With a further increase in the calcination temperature to 1373 K, the complete diffraction pattern of the spinel was recorded, with narrow and intense reflections due to a better crystallization.

Comparing the patterns of samples with different silicate contents, the higher the silicate loading, the more intense the forsterite phase diffraction lines were, while the temperatures required to form phases did not change. Previously,[39] we reported that the formation of the forsterite phase inhibited the formation of the rock-salt phase. This was clearly confirmed in the pattern of the sample with 62% silicates calcined at 1373 K, where only low rock-salt diffraction lines were observed, although this behavior may also be observed in the sample treated at 1173 K, namely the temperature used to prepare CPO catalysts.

These results showed that the presence of silicates in Ni/Mg/Al HTs did not change the decomposition pathway of the HT precursor very much, although it affected the amount of rock salt-type phase and, therefore, the rock-salt/spinel ratio (a key parameter for controlling the metallic particle properties), as well as the order of the spinel structure.

To gain insight into the effect of silicates in the formation of the spinel-type phase, a HT precursor without Mg^{2+} and containing 20% excess of silicates, *i.e.* a Ni/Al HT (Ni68), was studied. In this sample, Mg^{2+} ions were not available for forsterite formation, but the $NiAl_2O_4$ spinel could be formed. For comparison purposes, a Ni/Al HT with the same a.r.% but intercalated with carbonates was prepared (Ni68–CO_3). The diffraction patterns of the samples calcined at 1173 and 1373 K are shown in Fig. 2. The spinel formation and the sintering of NiO phases were delayed by silicates; indeed even at 1373 K some spinel reflections were missing in the diffraction pattern, thus confirming the formation of a defective and/or disordered phase. It may be hypothesized that an amorphous silico-aluminate formed during calcination, entrapped Al^{3+}, and hindered the spinel formation. On the other hand, when Mg^{2+} ions were present, the effect of the silicates on the spinel formation was reduced since silica reacted preferentially by forming the forsterite phase, although it was not fully avoided.

Silicates had an effect not only on crystalline phases, but also on textural properties.[39] The trend in both the specific surface area and the pore volume measured at different calcination steps (Table 1) was in agreement with those previously reported for carbonate-intercalated decomposition products.[47] Samples calcined at 773 K showed the highest surface areas; the higher the silicate content, the lower the surface area.

Lastly, the changes in Ni^{2+} reducibility during calcination treatment for the Ni8 sample containing 20% silicates were studied by H_2 TPR. The reduction profiles of the samples calcined at 773, 1023, and 1173 K are shown in Fig. 3. First of all, it should be pointed out that regardless of the calcination temperature, H_2 consumption took place above 900 K, making it possible to rule out the presence of free NiO. Two overlapping H_2 consumption peaks were registered at approximately 1060 and 1150 K for the sample calcined at 773 K; the intensity of the former peak decreased, while the latter seemed to increase by raising the calcination temperature to 1023 K. A single H_2 consumption peak at approximately 1223 K was recorded for the actual catalyst, *i.e.* the sample calcined at 1173 K.[13] Thus, in silicate-containing catalysts, even at moderate calcination temperatures (*i.e.* 773 K), Ni species were quite well stabilized in the Mg/Ni/Al oxide matrix, although an increase in calcination temperature caused a more difficult reduction of Ni^{2+} species.

3.2. Ni speciation in catalysts

The effect of Ni loading (Ni0, Ni2, Ni8, and Ni15) on the distribution of Ni species in actual catalysts (containing 20% excess silicates and obtained after calcination at 1173 K and reduction) was studied through a combination of XRD, TPR/TPO/TPR, XPS and XAS analyses.

Diffraction patterns in the 3–80° 2θ range showed an increased peak broadening, particularly for MgO- and spinel-type phases, with the Ni loading. To investigate whether Ni was dissolved into MgO- or spinel-type phases, high-resolution XRD patterns were collected in the 90–148° 2θ range. By increasing the Ni content, MgO reflections shifted progressively to higher 2θ values, thus indicating a shrinkage of the MgO cubic cell[48] due to the replacement of Mg^{2+} by Ni^{2+} (ionic radii

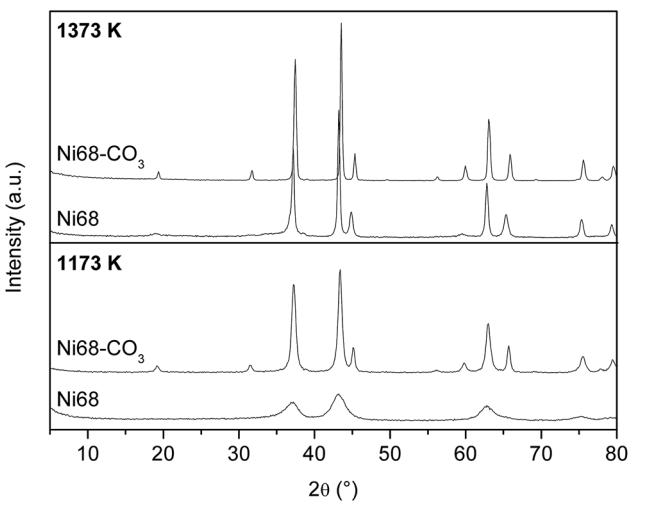

Fig. 2 XRD patterns of Ni/Al = 68/32 a.r.% samples intercalated with carbonates and silicates after calcination at 1173 K and 1373 K.

Table 1 Specific surface area values (S_{BET}) of Ni8 samples containing 20 and 62% excess of silicates calcined at selected temperatures for 12 h

$S_{BET}/m^2\ g^{-1}$	773 K	1023 K	1173 K	1373 K
Ni8-20	314	270	96	21
Ni8-62	293	233	87	18

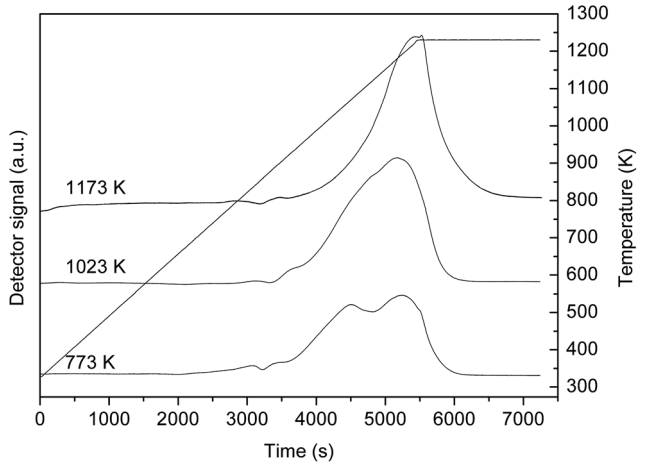

Fig. 3 H_2 TPR profiles of the Ni8 sample intercalated with 20% silicates after calcination at 773, 1023 and 1173 K.

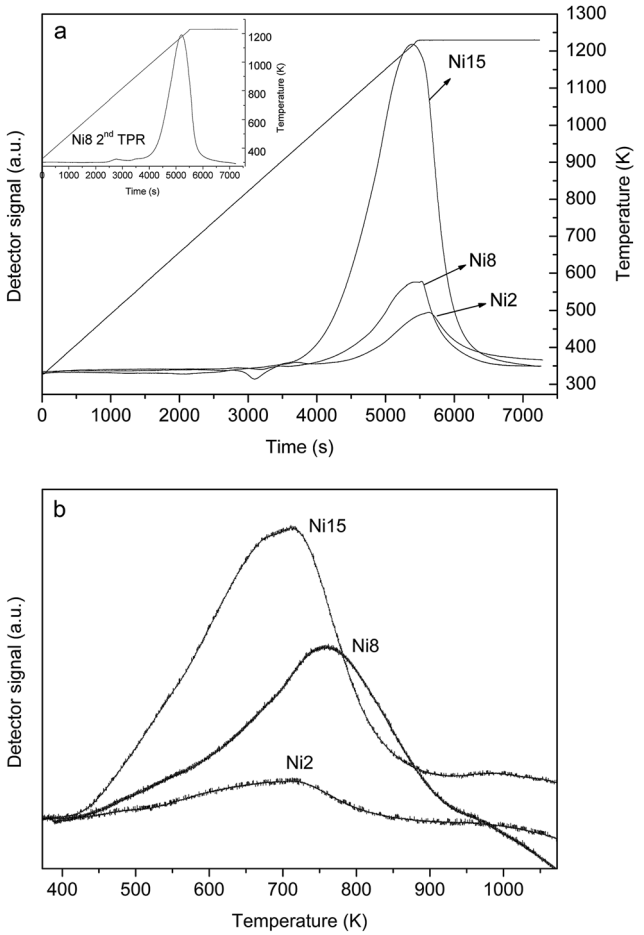

Fig. 4 H_2 TPR (a) and O_2 TPO (b) profiles of the catalysts with different Ni content (Ni 15, Ni8, Ni2). Inset in (a) second TPR after the oxidation analysis.

for octahedral Mg^{2+} and Ni^{2+} equal to 0.72 and 0.69 Å, respectively).[49] MgO cell parameters were, respectively: MgO, $a = 4.214 \pm 0.003$ Å; Ni0, $a = 4.209 \pm 0.003$ Å; Ni2, $a = 4.209 \pm 0.003$ Å; Ni8, $a = 4.201 \pm 0.006$ Å; Ni15, $a = 4.201 \pm 0.006$ Å.

Conversely, no shifts in the reflections due to the spinel phase were detected. A shrinkage of the $MgAl_2O_4$ unit cell was not apparent because $NiAl_2O_4$ is a partially inverse spinel whereas $MgAl_2O_4$ is a normal one; thus the substitution of Mg^{2+} by the smaller Ni^{2+} ion in octahedral (Oh) sites was compensated by the partial insertion of Ni^{2+}, replacing the smaller Al^{3+} ion, in tetrahedral (Td) sites (ionic radii for tetrahedral Ni^{2+} and Al^{3+} equal to 0.55 and 0.39 Å, respectively).[49]

The reduction and oxidation of Ni species was studied by H_2-TPR and O_2-TPO, namely by performing cycling TPR/TPO/TPR tests. During the first reduction cycle, the Ni loading slightly modified TPR profiles (Fig. 4a). The onset and maximum temperature of H_2-consumption curves shifted to lower temperatures by increasing the Ni content from 2 to 15 a.r.%. These results are consistent with the presence of Ni in a highly stabilized structure, MgO or $MgAl_2O_4$, with higher metal/support interactions by lowering the Ni content. TPO curves (Fig. 4b) were characterized by a complex, broad oxygen consumption in the 423–973 K range. It would appear that both low and high Ni-loaded catalysts, Ni2 and Ni15 respectively, oxidized more easily than the Ni8 catalyst.

The second TPR cycle confirmed the stability of Ni active phase; the main reduction peak was recorded at the same temperature observed in the first TPR (in the inset of Fig. 4a the profile of the Ni8 sample was shown as an example). A similar behavior was previously observed by Li and coworkers[50] and by Guil-López and coworkers,[51] who observed that catalysts with low Ni content maintained a constant reduction profile during 10 reduction–reoxidation cycles. It may be hypothesized that when Ni^0 was oxidized to Ni^{2+}, it did not segregate as NiO on the catalyst surface, but restored the species present in the starting sample, namely $Mg_{1-x}Ni_xO$ or $Ni_{x+y}Mg_{1-x}Al_{2-y}O_4$ solid solutions. The confinement of Ni^0 particles into mixed oxide nanoribbons[15] and/or small sizes of NiO would be conducive to this process, since there are more atoms at the interface promoting the solid–solid reaction.[52]

To study the role of the amount of Ni and the oxide matrix on the reduction/oxidation behavior, TPR/TPO/TPR profiles of high-loaded Ni/Al catalysts obtained from silicates and carbonates (Ni68 and Ni68–CO_3), previously characterized by XRD, were investigated (Fig. 5). The first reduction profile of the silicate-containing catalyst showed a single H_2 consumption at 1123 K, while for the carbonate-derived catalyst two overlapping peaks were recorded due to the reduction of NiO and $NiAl_2O_4$, respectively.[4] Slight changes occurred during the Ni68–CO_3 sample reduction/oxidation cycle and the peaks were better defined in the second TPR profile. Conversely for the silicate-containing Ni68 sample, a peak at low temperature appeared due to the formation of NiO particles, which interacted slightly with the support. Thus nickel loading and the nature of the oxide matrix played a key role in the stability of the Ni particles.

The XPS spectra of all the samples calcined at 1173 K contained Mg2p peaks at 50.4 ± 0.2 eV and Al2p at 74.4 ± 0.2 eV, in agreement with literature data for spinel-type structures[53] and Si2p at 102.3 ± 0.2 eV as for forsterite (Mg_2SiO_4).[54] $Ni2p_{3/2}$ at 856.6 ± 0.2 eV (FWHM about 2.8–3.2 eV) with a shake-up at

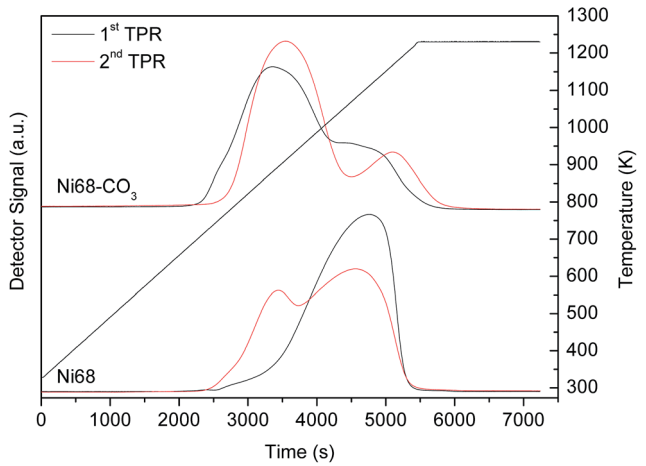

Fig. 5 Evolution of the TPR profiles during the TPR/TPO/TPR cycle for Ni/Al = 68/32 a.r.% samples containing carbonates and silicates calcined at 1173 K.

about 6.2 eV higher BE, was consistent with the presence of Ni^{2+} species.[55,56] When comparing $Ni2p_{3/2}$ BE values for NiO (854.5 eV),[56] $NiAl_2O_4$ (856.0–857.3 eV),[55] and NiO–MgO solid solution (855.7 eV)[57] with those of samples, the broad $Ni2p_{3/2}$ feature at 856.6 eV suggested the presence of surface Ni-containing species with different environments. It may be inferred that Ni^{2+} species were very likely present in surface $NiAl_2O_4$ or MgO solid solution or both.

The reduction treatment yielded changes in the Ni2p feature, whereas no changes either in BE or peak shape of all the other elements were observed. The shape and position of the Ni2p region detected in two sets of samples (Ni2 and Ni8) revealed the presence of Ni^0 as a major component, with a small amount of the oxidized phase. The Ni2p region could be resolved by a curve-fitting procedure into two doublets with $Ni(2p_{3/2})$ components at 852.8 eV (FWHM, 3.0 eV) and at 856.7 eV (FWHM, 4.5 eV; shake-up contribution 6.0 eV higher BE), attributed to Ni^0 and Ni^{2+}, respectively. The amount of surface species was in the range of 70–80% for Ni^0 and from 30–20% for Ni^{2+}, thus suggesting an incomplete reduction of the Ni species.

The surface composition, measured by the XPS-derived Ni2p/Mg2p (*n*Ni/*n*Mg), Ni2p/Al2p (*n*Ni/*n*Mg), and Mg2p/Al2p (*n*Mg/*n*Al) atomic ratios, did not follow the trend of the bulk composition. On all the samples, the surface concentrations of Ni and Al were higher than those expected on the basis of the bulk composition, revealing a high mobility of Ni- and Al-containing species toward the surface (Table 2), and supporting the presence of surface $NiAl_2O_4$. The strong decrease in the Ni2p peak intensity (about 50%) after reduction at 1023 K, resulted in a surface concentration close to that of the bulk (Table 2), indicating that heating caused an agglomeration of the surface species. Ni^0 metal particle size was around 12.1 nm, as revealed by TEM.[42]

The relevant structural data on the NiO, $NiAl_2O_4$, and Ni metal reference compounds are listed in Table 3. In order to reproduce the first shell of the EXAFS spectrum of the $NiAl_2O_4$ spinel, a partially inverse spinel with 1/4 of octahedral sites occupied by Ni^{2+} ions and 3/4 by Al^{3+} ions was considered,[58] fixing the ratio between octahedral and tetrahedral Ni^{2+} species to 1 : 3.

Table 2 Bulk and XPS-derived surface atomic composition for catalysts heated at 1073 K and after *in situ* treatment in flowing H_2/N_2 mixture

Samples		*n*Ni/*n*Mg	*n*Ni/*n*Al	*n*Mg/*n*Al
Ni0	Bulk	—	—	2.125
	Surface			1.870
Ni2	Bulk	0.030	0.062	2.062
	Surface	0.066	0.102	1.540
	H_2 surface	0.031	0.064	2.040
Ni8	Bulk	0.133	0.250	1.875
	Surface	0.258	0.349	1.347
	H_2 surface	0.091	0.128	1.820
Ni15	Bulk	0.283	0.468	1.656
	Surface	0.458	0.648	1.515

A comparison between FTs of the NiO and $NiAl_2O_4$ reference compounds (Fig. 6a) showed, for NiO, a first shell peak in the 1.2–2.1 Å range (due to the Ni–O contributions) much less intense than the second shell peak in the 2.1–3.0 Å range (due to the Ni–Ni contributions); for $NiAl_2O_4$, a first shell peak in the 1.0–2.1 Å range was much more intense than the second shell peak (mainly containing Ni–Al contributions). This was due to the fact that Al was lighter than Ni as a backscattering atom.

The FTs of the Ni*x* with $x = 2, 8, 15$ (Fig. 6b) were very similar, showing a first shell peak in the 1.1–2.1 Å range and second shell peaks in the 2.1–2.9 Å range, which were comparable in intensity. In agreement with XPS findings, this evidence suggested the presence of both NiO and $NiAl_2O_4$ in the samples. Structural information on the first coordination shell surrounding Ni atoms in terms of coordination numbers (N) and interatomic distances (Ni–O) obtained by fitting procedure are reported in Table 4. For the $NiAl_2O_4$ spinel phase, the Ni–O fitted distances indicate Ni sites in tetrahedral (Td) and octahedral (Oh) coordination; for the NiO phase, "Ni–O Oh" are the interatomic distances of the octahedral Ni sites. For the reduced samples, Ni–Ni are the fitted distances relative to the first coordination shell of the Ni metal phase.

Moreover, in order to obtain an indication of the relative amounts of NiO and $NiAl_2O_4$ oxides in the samples, the EXAFS signal [$\chi(k)$] was divided into two contributions by using the additive EXAFS relation:[59]

$$\chi_{total}(k) = x_{NiO}\chi_{NiO}(k) + x_{NiAl_2O_4}\chi_{NiAl_2O_4}(k)$$

Table 3 Structural parameters of the reference materials

Reference material	Atom pair	Interatomic distance R (Å)	Coordination number
Ni metal	Ni–Ni	2.49	12
NiO	Ni–O	2.09	6
$NiAl_2O_4$	Ni–O	1.96	6
$NiAl_2O_4$	Ni–O	1.83	4

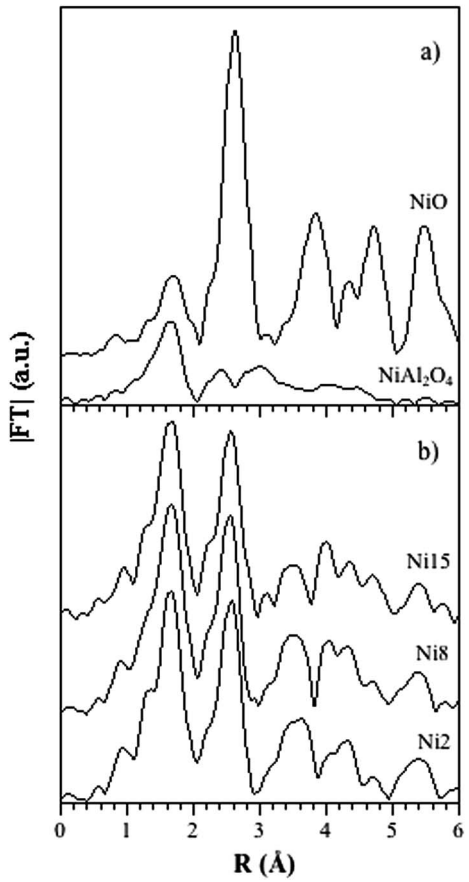

Fig. 6 Ni K-edge: Fourier transforms of the NiO and $NiAl_2O_4$ reference compounds (a) and Ni*x* with $x = 2$, 8, 15 samples (b).

where x is the fraction of the absorbing element in the NiO/$NiAl_2O_4$ phase. The x values (%), reported in Table 5, confirmed the presence of both NiO and $NiAl_2O_4$ in our samples, and it would appear that the amount of the latter increased with the Ni loading.

Table 4 First-shell EXAFS analysis of Ni*x* ($x = 2$, 8, 15) samples: coordination number ($N \pm 10\%$), interatomic distance ($R \pm 0.02$ Å), Debye–Waller factor ($\Delta\sigma^2 \pm 0.0005$ Å^2)

	Ni–O Td ($NiAl_2O_4$)			Ni–O Oh ($NiAl_2O_4$)			Ni–O Oh (NiO)		
Sample	N	R	$\Delta\sigma^2$	N	R	$\Delta\sigma^2$	N	R	$\Delta\sigma^2$
Ni2	0.7	1.82	0.0020	1.1	1.96	0.0005	5.1	2.09	0.0032
Ni8	0.9	1.84	0.0054	1.3	1.97	0.0011	4.5	2.09	0.0023
Ni15	1.5	1.84	0.0071	2.2	1.97	0.0027	3.9	2.09	0.0024

	Ni–O Oh (NiO)			Ni–Ni (Ni metal)		
Reduced sample	N	R	$\Delta\sigma^2$	N	R	$\Delta\sigma^2$
Ni2	2.4	2.06	0.0065	8.5	2.49	0.0038
Ni8	2.0	2.06	0.0069	8.7	2.49	0.0038

Fig. 7 shows the FTs of the Ni metal reference compound and of the reduced Ni2 sample as an example. An intense first shell peak in the 1.5–2.5 Å range, due to the Ni–Ni contributions, appeared with a shoulder in the lower region, due to Ni–O components still present, in agreement with XPS evidences. The results of the fitting procedure, Table 4, revealed that the $NiAl_2O_4$ phase was not present after reduction treatment, contrary to NiO. For the reduced samples the ratio (NiO : Ni^0) is about 30 : 70, quite similar to that obtained by XPS. A possible explanation for the presence of NiO after reduction may be the presence of a $Mg_{1-x}Ni_xO$ solid solution, in which Ni^{2+} was slightly reduced ($T_{redNi^{2+}} \geq 1073$ K), particularly if the solid solution was obtained at high temperature.[48]

The relative amount of Ni metal and NiO in the reduced samples (Table 5) was evaluated using the additive EXAFS relation:[59]

$$\chi_{total}(k) = x_{NiO}\chi_{NiO}(k) + x_{Ni^0}\chi_{Ni^0}(k)$$

where x is the fraction of the absorbing element in the NiO/Ni^0 phase. This evaluation was possible assuming no reduction in the Ni–Ni coordination of the reduced phase due to particle size effects.[42]

The data obtained by the EXAFS analysis found support in the fitting of the XANES experimental spectra of the reduced samples. The XANES experimental spectra collected for Ni^0 and NiO reference compounds were used as fingerprint models to perform a linear combination fit in the 8300–8390 eV range in order to reproduce the spectra of the reduced materials. XANES fit for the reduced Ni8 sample as an example is shown in Fig. 8. The relative amounts (%) of Ni^0 and NiO, reported in parentheses in Table 5, were in good agreement with those obtained by the EXAFS analysis, indicating that Ni8 sample was more reducible than Ni2 one (as also revealed by CO-DRIFTS analysis[42]).

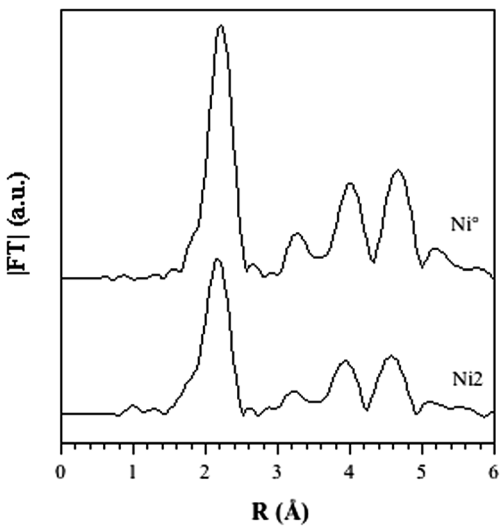

Fig. 7 Ni K-edge: Fourier transforms of the Ni metal reference compound and of the reduced Ni2 sample.

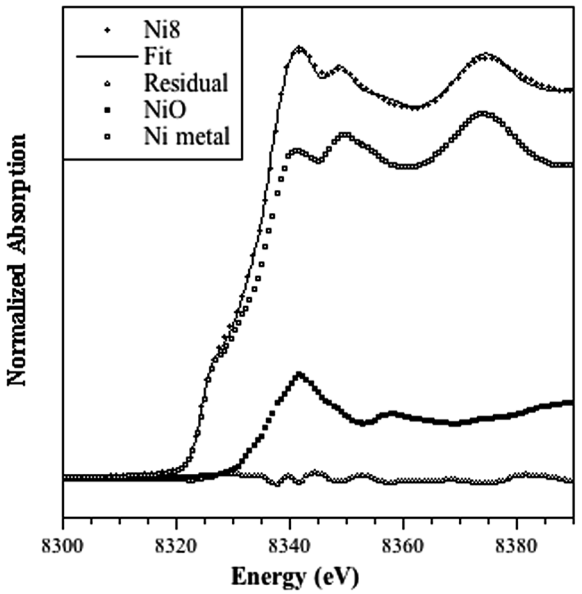

Fig. 8 Ni K-edge: XANES spectrum of the reduced Ni8 sample.

3.3. Concluding remarks

A fully and detailed picture of the Ni catalysts derived from HT compounds intercalated by silicates may be given by combining the data previously obtained by TPR, XPS, H_2 chemisorption, CO-DRIFTS, HRTEM and catalytic activity,[13,42] with TPR/TPO/TPR, XPS and XAS data reported in this work.

The Ni-containing species were distributed in MgO and $MgAl_2O_4$ phases in the calcined samples. The reduction treatment generated Ni^0 particles inside the oxide matrix (12.1 nm for Ni8).[42] However, in these freshly reduced catalysts, the presence of Ni^{2+} species in a $Ni_{1-x}Mg_xO$ solid solution, together with the embedment of some metallic particles inside the oxide matrix, decreased the amount of active sites available for the reaction, as confirmed by both CO and H_2 chemisorption;[42] for instance the dispersion values obtained by H_2 chemisorption were only 5.1 and 3.6% for Ni8 and Ni2 catalysts, respectively. During catalytic tests at high temperature (*i.e.* T_{oven} = 1023 K and $CH_4/O_2/He$ = 2/1/4 and 2/1/1 v/v), and whenever the Ni loading was high enough, namely in the Ni8 sample, CH_4 conversion and syngas selectivities above 90% were reached. Moreover, Ni^{2+} species into the $Ni_{1-x}Mg_xO$ phase could be further reduced and metallic particles segregated from the oxide matrix to the catalyst surface, without any sintering phenomena; consequently, the catalyst activated. On the other hand, for the Ni2 sample, the lower Ni loading in the catalyst and the larger amount of unreduced Ni^{2+} species in the $Ni_{1-x}Mg_xO$ phase, in comparison to Ni8, gave rise to a lower amount of available Ni^0 species and the deactivation of the catalyst by oxidation during harsh reaction conditions (*i.e.* T_{oven} = 1023 K and $CH_4/O_2/He$ = 2/1/4 and 2/1/1 v/v).

Table 5 Percentage of NiO and $NiAl_2O_4$ derived from EXAFS analysis of Ni*x* samples and percentage of NiO and Ni metal from EXAFS analysis of reduced samples; in parentheses, the data derived from XANES simulations. Inaccuracy was evaluated at around 10%

Sample	NiO (%)	$NiAl_2O_4$ (%)
Ni2	80	20
Ni8	75	25
Ni15	65	35

Reduced sample	NiO (%)	Ni^0 (%)
Ni2	35 (30)	65 (70)
Ni8	30 (20)	70 (80)

Although the characterization was performed on silicate-containing HT-derived catalysts, the results obtained may be also extended to other more conventional HT-derived Ni catalysts. In particular, it has been found that a careful control of the MgO/Al_2O_3 ratio and Ni content are the key parameters for controlling the Ni^{2+} reducibility and stability under reducing/oxidizing conditions.

A low Ni content must be preferred for an improvement of the reduction/oxidation cycle. It may play an important role in the catalytic partial oxidation of CH_4 in which, as a function of feed composition, the catalyst may be cyclically oxidized and reduced. Moreover, it may be important during the catalyst regeneration when, to remove contaminants such as carbon or sulfur, oxidation of the catalyst is used to recover the original activity. Thus, if the sample is stable the further reduction may restore the properties of the fresh sample.

On the other hand, increasing the Mg/Al ratio may aid the formation of the $Mg_{1-x}Ni_xO$ solid solution and, owing to its lower reducibility, the amount of available Ni^0 species and the catalytic performances may decrease. This problem may be overcome by an *in situ* activation of the catalyst with time-on-stream, as previously reported in the catalytic partial oxidation of CH_4.[13]

4. Conclusions

The introduction of silicates into the structure of Ni catalysts obtained from Ni/Mg/Al hydrotalcite-type precursors did not alter the decomposition temperatures, but modified the amount and properties of MgO and $MgAl_2O_4$ phases in the calcined samples because of the formation of Mg_2SiO_4 and the embedding of Al^{3+} cations in an amorphous silico-aluminate.

Regardless of the calcination temperature (773, 1023, or 1173 K) and the Ni loading (2, 8, or 15 a.r.%), Ni^{2+} species were well stabilized in the oxide matrix. In the actual catalysts they were distributed in both spinel and rock salt structures, although the latter were more abundant. The Ni loading and the oxide matrix determined the Ni^{2+} reducibility and the redox behavior. Low Ni-loaded catalysts contained a higher amount of difficult-to-reduce $Mg_{1-x}Ni_xO$, and therefore fewer metallic active sites in the reduced catalyst, albeit showing a better stability under reducing/oxidizing cycles.

Acknowledgements

The financial support from Ministero per l'Università e la Ricerca (MIUR) is gratefully acknowledged. ELETTRA beamline XAFS (Trieste, Italy) is acknowledged.

References

1 K. Takehira, T. Shishido, P. Wang, T. Kosaka and K. Takaki, *Phys. Chem. Chem. Phys.*, 2003, **5**, 3801–3810.
2 K. O. Christensen, D. Chen, R. Lødeng and A. Holmen, *Appl. Catal., A*, 2006, **314**, 9–22.
3 K. Takehira, T. Shishido, P. Wang, T. Kosaka and K. Takaki, *J. Catal.*, 2004, **221**, 43–54.
4 F. Basile, G. Fornasari, E. Poluzzi and A. Vaccari, *Appl. Clay Sci.*, 1998, **13**, 329–345.
5 A. Bhattacharyya, V. W. Chang and D. J. Schumacher, *Appl. Clay Sci.*, 1998, **13**, 317–328.
6 A. Olafsen, Å. Slagtern, I. M. Dahl, U. Olsbye, Y. Schuurman and C. Mirodatos, *J. Catal.*, 2005, **229**, 163–175.
7 A. Djaidja, S. Libs, A. Kiennemann and A. Barama, *Catal. Today*, 2006, **113**, 194–200.
8 A. Serrano-Lotina and L. Daza, *Appl. Catal., A*, 2014, **474**, 107–113.
9 K. Mette, S. Kühl, H. Düdder, K. Kähler, A. Tarasov, M. Muhler and M. Behrens, *ChemCatChem*, 2014, **6**, 100–104.
10 F. Basile, L. Basini, M. D'Amore, G. Fornasari, A. Guarinoni, D. Matteuzzi, G. Del Piero, F. Trifirò and A. Vaccari, *J. Catal.*, 1998, **173**, 247–256.
11 T. Shishido, M. Sukenobu, H. Morioka, M. Kondo, Y. Wang, K. Takaki and K. Takehira, *Appl. Catal., A*, 2002, **223**, 35–42.
12 Z. Jiang, J. Su, M. O. Jones, H. Shi, T. Xiao and P. P. Edwards, *Energy Fuels*, 2009, **23**, 1634–1639.
13 F. Basile, P. Benito, G. Fornasari, D. Gazzoli, I. Pettiti, V. Rosetti and A. Vaccari, *Catal. Today*, 2009, **142**, 78–84.
14 E. Ochoa-Fernández, C. Lacalle-Vilà, K. O. Christensen, J. C. Walmsley, M. Rønning, A. Holmen and D. Chen, *Top. Catal.*, 2007, **45**, 3–8.
15 R. Dehghan-Niri, J. C. Walmsley, A. Holmen, P. A. Midgley, E. Rytter, A. H. Dam, A. B. Hungria, J. C. Hernandez-Garrido and D. Chen, *Catal. Sci. Technol.*, 2012, **2**, 2476–2484.
16 M. K. Montañez, R. Molina and S. Moreno, *Int. J. Hydrogen Energy*, 2014, **39**, 8225–8237.
17 W. Fanga, S. Paula, M. Capron, F. Dumeignil and L. Jalowiecki-Duhamel, *Appl. Catal., B*, 2014, **152–153**, 370–382.
18 A. F. Lucrédio, J. M. Assaf and E. M. Assaf, *Biomass Bioenergy*, 2014, **60**, 8–17.
19 Q. Wang, W. Ren, X. Yuan, R. Mu, Z. Song and X. Wang, *Int. J. Hydrogen Energy*, 2012, **37**, 11488–11494.
20 M. Koike, D. Li, Y. Nakagawa and K. Tomishige, *ChemSusChem*, 2012, **5**, 2312–2314.
21 F. M. Josuinkas, C. P. B. Quitete, N. F. P. Ribeiro and M. M. V. M. Souza, *Fuel Process. Technol.*, 2014, **121**, 76–82.
22 F. Cavani, F. Trifirò and A. Vaccari, *Catal. Today*, 1991, **11**, 173–301.
23 J. R. H. Ross, *Surf. Defect Prop. Solids*, 1975, **4**, 34–67.
24 G. Fornasari, M. Gazzano, D. Matteuzzi, F. Trifirò and A. Vaccari, *Appl. Clay Sci.*, 1995, **10**, 69–82.
25 F. Basile, G. Fornasari, F. Trifirò and A. Vaccari, *Catal. Today*, 2002, **77**, 215–223.
26 S. Abelló, E. Bolshak and D. Montané, *Appl. Catal., A*, 2013, **450**, 261–274.
27 M. Muñoz, S. Moreno and R. Molina, *Int. J. Hydrogen Energy*, 2014, **39**, 10074–10089.
28 O. R. Macedo Neto, N. F. P. Ribeiro, C. A. C. Perez, M. Schmal and M. M. V. M. Souza, *Appl. Clay Sci.*, 2010, **48**, 542–546.
29 M. Muñoz, S. Moreno and R. Molina, *Int. J. Hydrogen Energy*, 2012, **37**, 18827–18842.
30 J. Ashok, Y. Kathiraser, M. L. Ang and S. Kawi, *Appl. Catal., B*, 2015, **172**, 116–128.
31 M. Gazzano, W. Kagunya, D. Matteuzzi and A. Vaccari, *J. Phys. Chem. B*, 1997, **101**, 4514–4519.
32 O. W. Perez-Lopez, A. Senger, N. R. Marcilio and M. A. Lansarin, *Appl. Catal., A*, 2006, **303**, 234–244.
33 A. Romero, M. Jobbágy, M. Laborde, G. Baronetti and N. Amadeo, *Catal. Today*, 2009, **149**, 407–412.
34 K. Nagaoka, A. Jentys and J. A. Lercher, *J. Catal.*, 2005, **229**, 185–196.
35 S. Casenave, H. Martinez, H. Guimon, A. Auroux, V. Hulea, A. Cordoneanu and E. Dumitriu, *Thermochim. Acta*, 2001, **379**, 85–93.
36 D. Tichit, F. Medina, B. Coq and R. Dutartre, *Appl. Catal., A*, 1997, **159**, 241–258.
37 K. Schulze, W. Makowski, R. Chyży, R. Dziembaj and G. Geismar, *Appl. Clay Sci.*, 2001, **18**, 59–69.
38 E. Bjørgum, D. Chen, M. G. Bakken, K. O. Christensen, A. Holmen, O. Lytken and I. Chorkendorff, *J. Phys. Chem. B*, 2005, **109**, 2360–2370.
39 S. Albertazzi, F. Basile, P. Benito, P. Del Gallo, G. Fornasari, D. Gary, V. Rosetti and A. Vaccari, *Catal. Today*, 2007, **128**, 258–263.
40 T. Baskaran, R. Kumaravel, J. Christopher and A. Sakthivel, *RSC Adv.*, 2013, **3**, 16392–16398.
41 T. Baskaran, R. Kumaravel, J. Christopher and A. Sakthivel, *RSC Adv.*, 2014, **4**, 11188–11196.
42 P. Benito, V. Dal Santo, V. de Grandi, M. Marelli, G. Fornasari, R. Psaro and A. Vaccari, *Appl. Catal., B*, 2015, **179**, 150–159.
43 T. J. B. Holland and S. A. T. Redfern, *J. Appl. Crystallogr.*, 1997, **30**, 84.
44 C. D. Wagner, L. E. Davis, M. V. Zeller, J. A. Taylor, R. H. Raymond and L. H. Gale, *Surf. Interface Anal.*, 1981, **3**, 211–225.
45 M. Newville, *J. Synchrotron Radiat.*, 2001, **8**, 322–324.
46 K. E. Sickafus, *J. Nucl. Mater.*, 2002, **300**, 151–160.
47 P. Benito, M. Herrero, F. M. Labajos and V. Rives, *Appl. Clay Sci.*, 2010, **48**, 218–227.
48 A. Cimino and F. S. Stone, *Adv. Catal.*, 2002, **47**, 141–306.
49 R. D. Shannon, *Acta Crystallogr., Sect. A: Cryst. Phys., Diffr., Theor. Gen. Crystallogr.*, 1976, **32**, 751–767.
50 D. Li, I. Atake, T. Shishido, Y. Oumi, T. Sano and K. Takehira, *J. Catal.*, 2007, **250**, 299–312.

51 R. Guil-López, V. La Parola, M. A. Peña and J. L. G. Fierro, *Catal. Today*, 2006, **116**, 289–297.
52 B. Li, K. Maruyama, M. Nurunnabi, K. Kunimori and K. Tomishige, *Ind. Eng. Chem. Res.*, 2005, **44**, 485–494.
53 A. H. Padsmari, A. Venugopal, V. Durga Kumari, K. S. Rama Rao and P. Kanta Rao, *J. Mol. Catal. A: Chem.*, 2002, **188**, 255–265.
54 K. Okada, Y. Kameshima and A. Yasumori, *J. Am. Ceram. Soc.*, 1998, **81**, 1970–1972.
55 S. Velu, K. Suzuki, M. Vijayara, S. Barman and C. S. Gopinath, *Appl. Catal., B*, 2005, **55**, 287–299.
56 A. P. Grosvenor, M. C. Biesinger, R. St. C. Smart and N. S. McIntyre, *Surf. Sci.*, 2006, **600**, 1771–1779.
57 A. Cimino, D. Gazzoli, V. Indovina, G. Moretti, M. Occhiuzzi and F. Pepe, *Top. Catal.*, 1999, **8**, 171–178.
58 G. Blasse, Crystal chemistry and some magnetic properties of mixed oxides with spinel structure, *Philips Res. Rep.*, 1964, (3), 22.
59 G. U. Kulkarni, G. Sankar and C. N. R. Rao, *J. Catal.*, 1991, **131**, 491–501.